ACS APPLIED MATERIALS & INTERFACES

www.acsami.org

Research Article

Overcoming the Miscibility Gap of GaN/InN in MBE Growth of Cubic $In_xGa_{1-x}N$

Mario Fabian Zscherp, Silas Aurel Jentsch, Marius Johannes Müller, Vitalii Lider, Celina Becker, Limei Chen, Mario Littmann, Falco Meier, Andreas Beyer, Detlev Michael Hofmann, Donat Josef As, Peter Jens Klar, Kerstin Volz, Sangam Chatterjee, and Jörg Schörmann*

Cite This: *ACS Appl. Mater. Interfaces* 2023, 15, 39513−39522

Read Online

ACCESS | Metrics & More | Article Recommendations | Supporting Information

ABSTRACT: The lack of internal polarization fields in cubic group-III nitrides makes them promising arsenic-free contenders for next-generation high-performance electronic and optoelectronic applications. In particular, cubic $In_xGa_{1-x}N$ semiconductor alloys promise band gap tuning across and beyond the visible spectrum, from the near-ultraviolet to the near-infrared. However, realization across the complete composition range has been deemed impossible due to a miscibility gap corresponding to the amber spectral range. In this study, we use plasma-assisted molecular beam epitaxy (PAMBE) to fabricate cubic $In_xGa_{1-x}N$ films on c-GaN/AlN/3C-SiC/Si template substrates that overcome this challenge by careful adjustment of the growth conditions, conclusively closing the miscibility gap. X-ray diffraction reveals the composition, phase purity, and strain properties of the $In_xGa_{1-x}N$ films. Scanning transmission electron microscopy reveals a CuPt-type ordering on the atomistic scale in highly alloyed films with $x(\mathrm{In}) \approx 0.5$. Layers with much lower and much higher indium content exhibit statistical distributions of the cations Ga and In. Notably, this CuPt-type ordering results in a spectrally narrower emission compared to that of statistically disordered zincblende materials. The emission energies of the films range from 3.24 to 0.69 eV and feature a quadratic bowing parameter of $b = 2.4$ eV. In contrast, the LO-like phonon modes that are observed by Raman spectroscopy exhibit a one-mode behavior and shift linearly from c-GaN to c-InN.

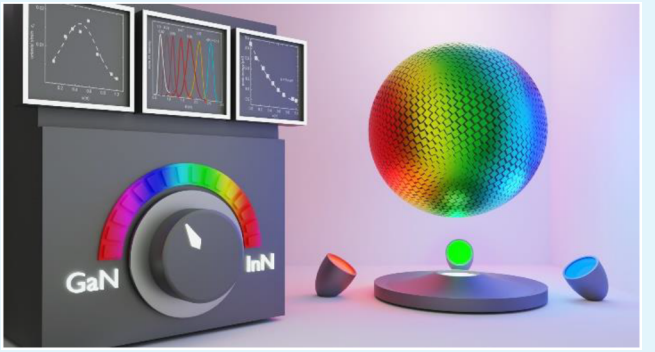

KEYWORDS: *molecular beam epitaxy, $In_xGa_{1-x}N$, strain, miscibility, cubic III-nitrides, TEM, optical properties*

INTRODUCTION

Light-emitting semiconductor devices with sufficient quantum efficiencies that are able to operate across the complete visible spectrum and are based on the same epitaxially grown semiconductor alloy system will disruptively change the landscape of optoelectronic applications and devices. They will eliminate the need for phosphors in white light-emitting diodes (LEDs) and potentially yield multiple color lasers or illuminators such as micro-LEDs.[1] Zincblende $In_xGa_{1-x}N$ is a prime contender for these tasks, as its direct band gap is tunable from the near-ultraviolet[2,3] toward the near-infrared.[4−6] Unlike the thermodynamically stable hexagonal wurtzite phase, the cubic crystal structure is free of internal piezoelectric fields,[7−10] which commonly reduce the radiative recombination of electrons and holes.[11] This advantage becomes more important with increasing In content, as a larger In content also increases the piezoelectric fields and greatly reduces the efficiency of green and amber h-$In_xGa_{1-x}N$-based LEDs.

However, growing metastable c-$In_xGa_{1-x}N$ films that have good epitaxial quality is difficult due to largely different lattice constants,[4,12] significantly different growth temperatures for the two binary compounds, and a lack of substrates for homoepitaxy. As a result, reports of the phase-pure growth of c-$In_xGa_{1-x}N$ with more than 30% In content are scarce, and numerous works predict[13,14] and report[15−17] spinodal decomposition with the formation of an additional In-rich phase. In most cases, c-$In_xGa_{1-x}N$ is heteroepitaxially grown on c-GaN. This interface can induce a significant amount of strain in the c-$In_xGa_{1-x}N$ layers, depending on the indium content and the layer thickness. As a result, the cubic crystal symmetry is distorted tetragonally, and in-plane and out-of-plane lattice constants deviate from each other. Neglecting this distortion usually leads to an overestimation of the indium content by up

Received: May 3, 2023
Accepted: July 21, 2023
Published: August 2, 2023

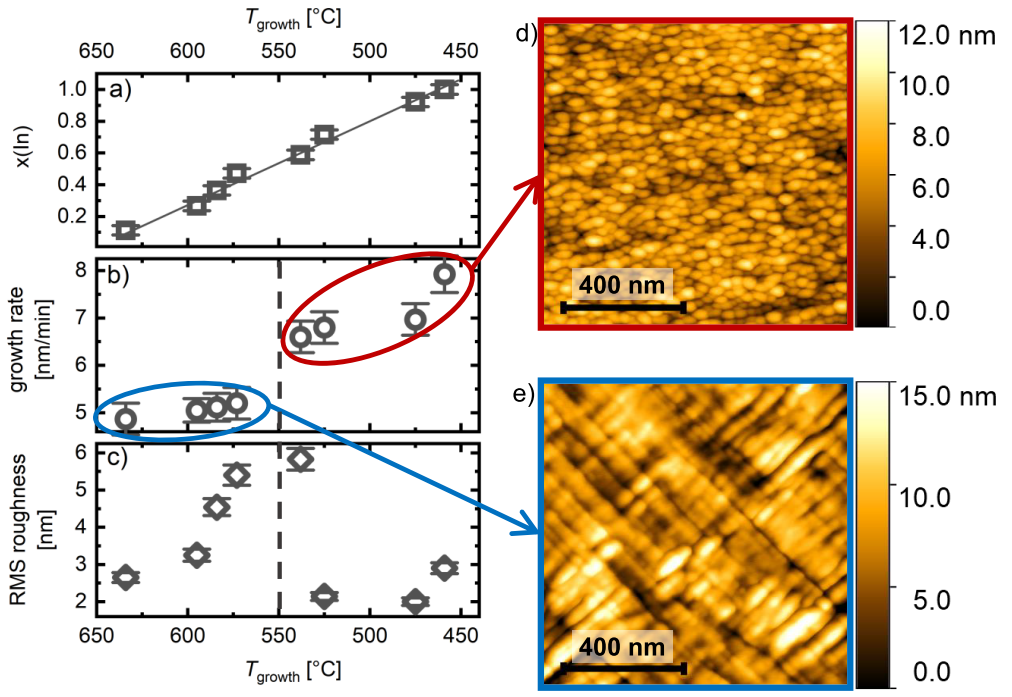

Figure 1. Impact the growth temperature T_{growth} has on the c-$In_xGa_{1-x}N$ epitaxial layer. As T_{growth} decreases, (a) the indium content increases linearly, (b) the growth rate showcases two distinct regimes, and (c) the roughness increases to a maximum (though it is lowest at low temperatures). Two 1 × 1 μm^2 AFM scans show the morphology of (d) the low-temperature regime and (e) the high-temperature regime.

to 20%. Therefore, it is important to consider such strain in order to understand the impact indium content has on the optical properties of c-$In_xGa_{1-x}N$.

In this work, we report phase-pure cubic $In_xGa_{1-x}N$ layers with $0 \leq x(In) \leq 1$ grown on c-GaN/AlN/3C-SiC/Si(001) templates by plasma-assisted molecular beam epitaxy (PAMBE). We demonstrate the continuous tunability of the indium content by carefully adjusting the growth temperature and the metal fluxes. Furthermore, we emphasize the role of strain in enabling full miscibility of c-GaN and c-InN. Comprehensive characterization of the layers illustrates the impact indium content has on the nanoscopic crystal lattice and on the optical response of the cubic $In_xGa_{1-x}N$ layers.

EXPERIMENTAL SECTION

Cubic $In_xGa_{1-x}N$ layers are grown on c-GaN templates at T_{growth}, ranging from 460 to 630 °C, by PAMBE. All epitaxial layers feature a thickness of approximately 80−100 nm. The indium contents x(In) of the various layers grown are 0.11, 0.27, 0.36, 0.47, 0.59, 0.72, 0.92, and 1. The c-GaN templates, with thicknesses of approximately 600 nm, are grown using an 8 nm c-AlN buffer[18] on commercial 3C-SiC/Si(001) pseudo substrates (NovaSiC). The MBE chamber (Riber Compact 12) is equipped with standard effusion cells and an Oxford Applied Research HD25 radio frequency plasma source. The growth surface is monitored by in situ reflection high energy electron diffraction (RHEED). For c-$In_xGa_{1-x}N$ growth, the sensitivity-corrected beam equivalent pressures (BEP) of gallium and indium are varied between 1.4×10^{-8} and 1.1×10^{-7} mbar and between 9.2×10^{-8} and 2.5×10^{-7} mbar, respectively.

High-resolution X-ray diffraction (HRXRD), using a Rigaku SmartLab diffractometer that operates a 9 kW rotating Cu anode, provides the initial structural characterization, including the determination of the indium content. The thickness of the c-$In_xGa_{1-x}N$ layers is determined from cross-sectional scanning electron microscopy images, obtained with a JEOL JSM-7001F instrument, and confirmed by X-ray reflectivity measurements. A Bruker Multimode 8 atomic force microscope (AFM), operating in the ScanAsyst Air mode and using Bruker SCANASYST-AIR probes, yields the surface morphology. Gwyddion software is used for image processing and deriving the root-mean-square (RMS) roughness.

Because the optical properties are of particular interest for potential future applications, we studied the low-temperature ($T \approx 20$ K) photoluminescence (PL) of the samples. Three different measurement setups are used to cover the large variation in emission energies, all of which feature a laser diode at 405 nm for excitation. Samples with x(In) < 0.5 are measured using an excitation power of $P_{exc,1} = 6.9$ mW and a thermoelectrically (TE) cooled, ultraviolet-optimized back-illuminated CCD camera. Samples with higher In content ($0.5 < x(In) < 0.75$) are measured using $P_{exc,2} = 22$ mW and a 1.7 μm TE-cooled InGaAs array detector. For samples with x(In) > 0.75, a 2.2 μm TE-cooled InGaAs array detector is used with $P_{exc,3} = 23$ mW.

The scanning transmission electron microscopy (STEM) investigations in the present study employ a double-aberrations-corrected JEOL JEM-2200FS microscope, operating at 200 kV with an annular dark-field (ADF) detector. Two imaging modes are used, namely the high-angle ADF (HAADF) and the low-angle ADF (LAADF) imaging modes. The former mode is utilized to obtain high-resolution images of the material's structure, while the latter mode is used to visualize the defects in the sample. Energy-dispersive X-ray spectroscopy (EDX) is used to generate composition maps and determine the local In concentration.

Raman spectra are recorded at room temperature using a Renishaw inVia Raman spectrometer combined with a Leica optical microscope in a backscattering geometry. A 405 nm line from a C-FLEX laser combiner (HÜBNER Photonics) is used as the excitation source. The laser power is typically a few milliwatts. A 50× objective is used to focus the laser light onto the sample and collect the scattered light. The collected light is dispersed by a 1800 lines per millimeter diffraction grating in the spectrometer and is then focused onto a charge-coupled device (CCD) detector.

RESULTS AND DISCUSSION

The III/III and III/V ratios are adjusted carefully in order to grow c-$In_xGa_{1-x}N$ across the whole composition range. In

https://doi.org/10.1021/acsami.3c06319
ACS Appl. Mater. Interfaces 2023, 15, 39513−39522

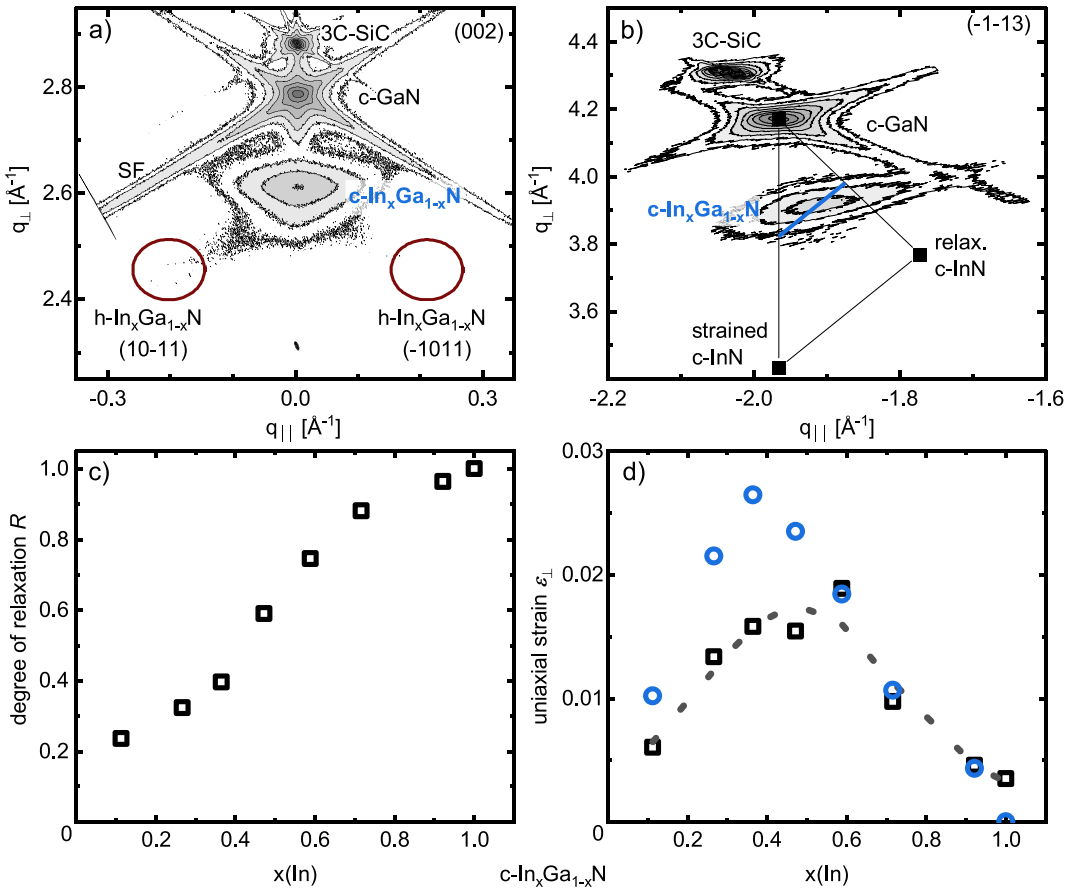

Figure 2. Selected reciprocal space maps of a sample with x(In) = 0.47, centered at (a) the symmetric (002) reflection and (b) the asymmetric (−1−13) reflection of c-GaN. The space maps reveal a pure cubic phase and a single, but strained, c-In$_x$Ga$_{1-x}$N phase. (c) The degree of relaxation continuously increases with x(In), whereas (d) the uniaxial strain is highest for intermediate indium content (the dashed line serves as a guide for the eye). Black squares represent the strain calculated using the $2\theta-\omega$ scans, and the blue circles denote the strain derived from the degree of relaxation using the elastic constants of the binary compounds.

general, metal-rich growth conditions lead to smooth surfaces and phase-pure cubic epitaxial layers,[18,19] whereas the In/Ga ratio is vital for tuning the alloy's composition. However, the growth temperature T_{growth} governs the maximum In content of the thin film due to the low binding energy of In−N. The impact of T_{growth} on the growth rate, the morphology, and the surface roughness of the c-In$_x$Ga$_{1-x}$N layers is detailed in Figure 1.

Figure 1a shows that the In content x(In) increases linearly as the growth temperature decreases. Next, we observe two distinct growth regimes, where a sharp increase in the growth rate from 5.2 to 6.6 nm/min occurs at $T_{growth} \cong 550$ °C (Figure 1b). Correspondingly, AFM imaging reveals two different surface morphologies that are dependent on the growth temperature. For low temperatures ($T_{growth} < 550$ °C), we observe small, round crystallites ($d_{cryst} \approx 50$ nm, Figure 1d). In contrast, for high temperatures ($T_{growth} > 550$ °C), the c-In$_x$Ga$_{1-x}$N surface exhibits elongated crystallites (Figure 1e). Additionally, the RMS roughness increases with decreasing temperature, reaching a maximum value of 5.8 nm at T_{growth} = 538 °C (Figure 1c). However, the height of the round crystallites decreases rapidly for even lower temperatures and high In content, yielding smooth surfaces with an RMS roughness of approximately 2 nm.

The differences in morphology are in concordance with in situ RHEED observations (Figure S1) at the initial c-In$_x$Ga$_{1-x}$N growth. In the high-temperature regime, the streaky pattern of c-GaN is retained for several minutes. For lower growth temperatures, the RHEED pattern immediately shifts to oval-shaped reflections with the start of c-In$_x$Ga$_{1-x}$N growth. This indicates different nucleation processes of c-In$_x$Ga$_{1-x}$N on c-GaN for these two cases. Overall, these results highlight the crucial role growth temperature plays on the indium content, growth rate, and morphology.

Mapping the reciprocal space of both the symmetric (002) and asymmetric (−1−13) reflections by using HRXRD is essential for investigating and validating the crystal structure of the c-In$_x$Ga$_{1-x}$N alloys. In particular, any hexagonal inclusions are important to quantify, as they can nucleate on cubic (111) facets. Figure 2a shows an exemplary reciprocal space map centered at the (002) reflection of c-GaN. The red circles mark the expected position of the (10−11) and (−1011) reflections of hexagonal In$_x$Ga$_{1-x}$N. The intensity ratio of the hexagonal {10−11} reflection and the cubic (002) reflection is an indication of the proportion of hexagonal inclusions. This ratio is below 2% for all of the ternary c-In$_x$Ga$_{1-x}$N samples in this study, which confirms the purity of the cubic zincblende phase. Furthermore, we do not observe any secondary c-In$_x$Ga$_{1-x}$N reflections on the (002) or (−1−13) space maps, which would

https://doi.org/10.1021/acsami.3c06319
ACS Appl. Mater. Interfaces 2023, 15, 39513−39522

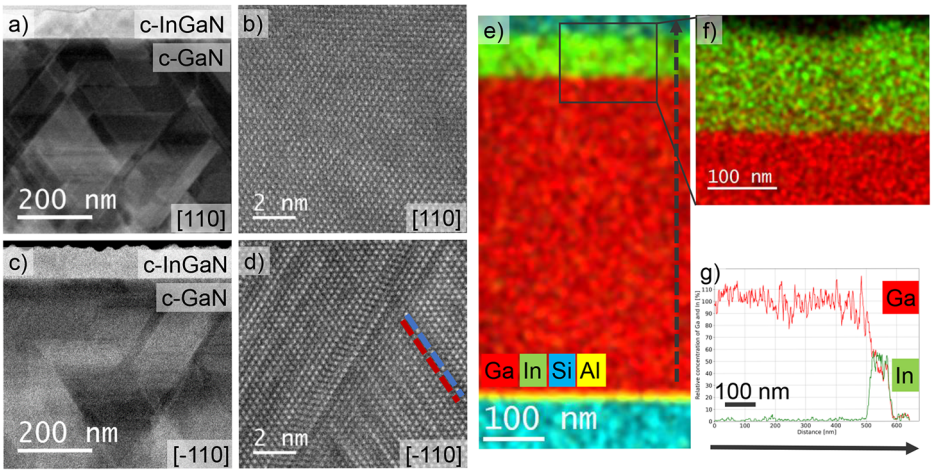

Figure 3. (a, c) STEM measurements of a sample with x(In) = 0.47; the defect-sensitive LAADF images show propagating stacking faults in the (a) [110] and (c) [−110] directions. (b, d) HR-HAADF images that reveal short-range CuPt-type ordering, as indicated by the red and blue dashed lines. (e, f) EDX imaging that confirms an overall homogeneous chemical composition. (g) Quantitative EDX, performed as a line scan along the black dashed line in (e), verifies the indium concentration obtained by HRXRD.

have implied spinodal decomposition into a Ga-rich and an In-rich phase, regardless of the In content. This demonstrates the full miscibility of the c-$In_xGa_{1-x}N$ alloys. The line widths of the ω-rocking curves of the (002) c-$In_xGa_{1-x}N$ reflection range from 30 to 140 arcmin, depending on the composition.[20]

Strain is another aspect of the crystal structure that requires consideration, in addition to establishing the phase purity of the c-$In_xGa_{1-x}N$ layers. For example, a standard $2\theta-\omega$ scan along [002] will be misleading in determining the indium content of partially strained c-$In_xGa_{1-x}N$ epitaxial layers. This is because [002] is only related to the out-of-plane lattice constant $a_\perp$; thus, this kind of scan can lead to an overestimation of the In content by up to 20%. Conversely, measuring the asymmetric reciprocal space maps of the (−1−13) reflection avoids any overestimation. This is because the (−1−13) reflections are related to both the in-plane and the out-of-plane lattice constants. Comparing the position of the c-$In_xGa_{1-x}N$ reflection to the positions of c-GaN, the fully relaxed c-InN, and the fully strained c-InN (Figure 2b) allows one to assess the true In content and the theoretical relaxed lattice constant a_{relax} according to Vegard's law. Using the in-plane lattice constant $a_\parallel$, the degree of relaxation R relative to the c-GaN substrate is given by[21]

$$R = \frac{a_\parallel - a_{GaN}}{a_{relax} - a_{GaN}} \quad (1)$$

Furthermore, the deviation of $a_\perp$ from a_{relax} determines the uniaxial out-of-plane strain $\varepsilon_\perp$:

$$\varepsilon_\perp = \frac{a_\perp - a_{relax}}{a_{relax}} \quad (2)$$

Overall, the degree of relaxation increases with increasing x(In) (Figure 2c) due to an increasing lattice mismatch. This lattice mismatch causes a decrease in the critical thickness and, thus, faster relaxation.

In contrast, the uniaxial out-of-plane strain is highest for intermediate Ga and In contents (Figure 2d). To verify the consistency of these results, we calculated the out-of-plane strain by using two different approaches. In Figure 2d, the black squares represent the measured strain using eq 2, with $a_\perp$ having been obtained via $2\theta-\omega$ scans. The blue circles denote the calculated strain derived from the degree of relaxation using the linearly interpolated elastic constants[21,22] of the binary compounds.[23,24] For intermediate x(In), it was found that the measured strain is lower than predicted by the elastic constants. This implies that the c-$In_xGa_{1-x}N$ layers with those compositions are not stress-free and that the elastic medium approximation is not completely accurate.[21] In both cases, the trend of the uniaxial strain as a function of the In content resembles that of the miscibility gap in the c-GaN/InN phase diagram.[13,14] Furthermore, theoretical calculations of the mixing free energy predict that spinodal decomposition is suppressed in fully strained c-$In_xGa_{1-x}N$ layers on c-GaN.[13,25] Even though the c-$In_xGa_{1-x}N$ thin epitaxial films in this work are only partially strained (Figure 2c), the uniaxial strain is highest for the very compositions for which thermodynamics favors decomposition. This indicates that the strong uniaxial strain at intermediate x(In) is sufficient to counteract the predicted spinodal decomposition and is the reason for the presented full miscibility of our c-$In_xGa_{1-x}N$ layers.

The high structural quality of the layers is confirmed by STEM images in both the [110] and [−110] directions. Exemplary images of a sample with x(In) = 0.47 reveal its atomic arrangement, defects, and composition. It is known that extended defects such as stacking faults are a major cause of performance loss in device applications.[26] Figure 3a,c show defect-sensitive LAADF-STEM images of c-$In_xGa_{1-x}N$ on c-GaN along the two perpendicular directions. The majority of the stacking faults (SF) in the c-$In_xGa_{1-x}N$ layer in the [110] direction (Figure 3a) originate in the c-GaN layer and penetrate the GaN/$In_xGa_{1-x}N$ interface. Those stacking faults form at the interfaces of 3C-SiC/AlN/GaN and propagate through the entire epitaxial layer if no SF annihilation process occurs.[18,27−29] Therefore, reducing the number of SFs in the c-GaN substrate should also decrease the SF concentration in the c-$In_xGa_{1-x}N$ layer. Apart from the SFs, the HR-HAADF image (Figure 3b) of c-$In_xGa_{1-x}N$ shows the expected zincblende structure.

In contrast, the LAADF image of the [−110] direction (Figure 3c) shows fewer defects in c-GaN, and the c-$In_xGa_{1-x}N$ layer appears to be homogeneous. Nevertheless, the corresponding HR-HAADF image (Figure 3d) of the c-

https://doi.org/10.1021/acsami.3c06319
ACS Appl. Mater. Interfaces 2023, 15, 39513−39522

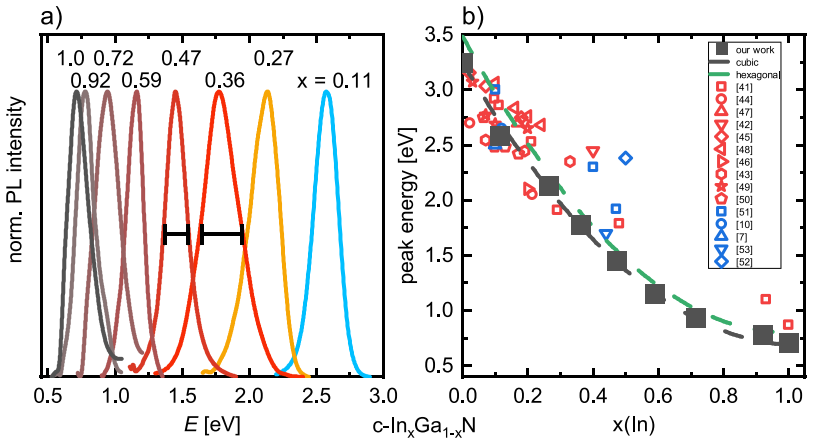

Figure 4. (a) Normalized low-temperature ($T \approx 20$ K) photoluminescence spectra of c-$In_xGa_{1-x}N$ over the whole composition range, where x denotes indium content. (b) Peak emission energy vs x(In), where the black squares denote data points of this work, the red symbols refer to the emission energies of bulk c-$In_xGa_{1-x}N$, and the blue symbols refer to the quantum structures. All data besides the black squares are taken from the literature. The bowing of the peak emission energy with x(In) is best described by a bowing coefficient of b = 2.4 eV (dashed black line).

$In_xGa_{1-x}N$ layer reveals a parallel periodic arrangement of darker and brighter contrast along the [111] planes, which are indicated by the red and blue dashed lines, respectively. These can be assigned to In- and Ga-rich regions, respectively, based on the atomic number (Z) sensitivity of the STEM imaging. Similar arrangements, where every other layer shows brighter contrast, are known as CuPt-type ordering in the literature.[30,31] However, the ordering observed in our samples is less periodic. Notably, this ordering is visible only in one of the two viewing directions (Figure 3d), but not in the perpendicular direction (Figure 3b). This implies the formation of sheets of In-rich and In-poor regions, rather than chains. The observed contrast would also be compatible with stacking faults that are buried in the viewing direction within the TEM sample. However, we think this is very unlikely, since the TEM sample is rather thin compared to the extensions of the stacking faults. Thus, the probability of finding a buried stacking fault would be very low. Moreover, a corresponding sample with x(In) = 0.21 does not show these intensity fluctuations on the {111} planes (Figure S2). CuPt-type ordering has already been observed in other highly alloyed ternary zincblende III−V materials, such as $InAs_xSb_{1-x}$[32] and $Ga_xIn_{1-x}P$.[33−35] For cubic nitride alloys, this kind of ordering has not been experimentally observed to date. Nonetheless, theoretical studies of alloy energies using a cluster expansion method predict the formation of ordered phase structures in cubic nitride alloys due to strain.[36,37] This prediction is consistent with the presented data, considering the strong uniaxial strain for samples with intermediate In content (Figure 2d).

EDX imaging of a cross section of a 3C-SiC/AlN/GaN/$In_xGa_{1-x}N$ sample with x(In) = 0.47 (Figure 3e) confirms the homogeneous chemical composition of the c-$In_xGa_{1-x}N$ layer (Figure 3f) on larger scale lengths. Quantitative EDX analysis (Figure 3g) yields an indium content of 0.49 ± 0.12, which is in excellent agreement with the value obtained from HRXRD.

So far, the analysis of the XRD reciprocal space maps and the EDX data gives evidence of the growth of partially relaxed c-$In_xGa_{1-x}N$ films on c-GaN/AlN/3C-SiC/Si templates over the complete composition range. LAADF investigations reveal the distribution of the SFs in the [110] and [−110] directions, and HR-HAADF images reveal an atomistic scale CuPt-type ordering in the highly alloyed samples ($x \approx 0.5$). Next, we investigate the impact of these features on the optical properties of the films by low-temperature photoluminescence spectroscopy and ambient-temperature micro-Raman spectroscopy.

Figure 4a shows the low-temperature photoluminescence (PL) spectra of the c-$In_xGa_{1-x}N$ films for compositions ranging from x(In) = 0.11−1.0. All spectra exhibit broad, singular emission peaks with a full width at half-maximum (FWHM) of approximately 150−300 meV. Including pure c-GaN,[18] the emission energies range from 3.24 to 0.71 eV, thus covering the spectral range from the near-ultraviolet (382 nm) to the near-infrared (1750 nm). The presented PL peak positions and corresponding literature data are plotted in Figure 4b as a function of the alloy composition. The presented c-$In_xGa_{1-x}N$ data (filled black squares) are ∼200 meV lower in energy for low x(In)[38] and ∼100 meV lower in energy for intermediate and high x(In)[39,40] compared to data for h-$In_xGa_{1-x}N$ films taken from the literature (green dashed line[39,40]). This roughly accounts for the difference in the band gap energies between the two structural modifications.[2−6,39] Notably, while several publications report bulk cubic $In_xGa_{1-x}N$ alloys with compositions up to 45% indium,[41−43] data for $x > 0.9$ are more scarce.[41] We go beyond these state-of-the-art reporting by obtaining emissions across the entire composition range, including the range between x(In) = 0.5 and 0.9. A quadratic bowing coefficient and the binary emission energies E(GaN) = 3.24 eV[3,18] and E(InN) = 0.69 eV[4] describe the entire composition range according to

$$E(In_xGa_{1-x}N) = E(GaN)(1 - x) + E(InN)x - bx(1 - x) \quad (3)$$

A bowing coefficient of b = 2.4 eV yields the best fit (dashed black line in Figure 4b). This value is slightly lower than the bowing of the emission energy in hexagonal $In_xGa_{1-x}N$ ($b \approx$ 2.8 eV).[39,40] Compared to other cubic $In_xGa_{1-x}N$ epilayers, the emission energies reported here for low indium content (x(In) < 0.3) align rather well with other bulk-like thin film samples.[41,43−50] For larger alloy compositions (0.3 < x(In) < 0.5), reports on the optical properties of c-$In_xGa_{1-x}N$ are sparse. We observe emission peaks at significantly lower energies than those of other c-$In_xGa_{1-x}N$ layers[41−43] or multi quantum wells.[51−53] The most recent study, ref 54, determines a significantly smaller bowing of b = 1.4 eV by ellipsometry measurements, which might be caused by the somewhat higher

https://doi.org/10.1021/acsami.3c06319
ACS Appl. Mater. Interfaces 2023, 15, 39513−39522

energy values that are measured in the very highly alloyed samples with x(In) > 0.9 and the lack of data for x(In) > 0.5 (see Figure 4b). The discrepancies may also arise from the fact that our emissions may be caused by recombinations that are localized in the potential valleys of the alloys, which ellipsometry may be less sensitive to.

Investigating the photoluminescence line shape in more detail reveals that its FWHM (Figure 5) increases for alloy

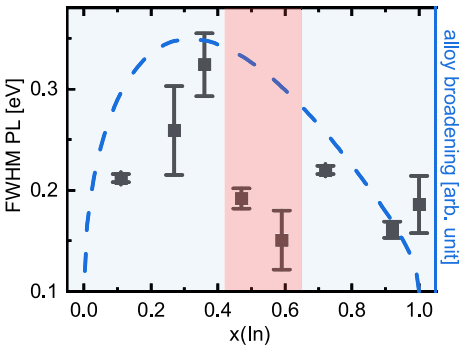

Figure 5. The FWHM values of the low-temperature PL measurements vs x(In). The blue dashed line represents the calculated alloy broadening due to the statistical occupation of the cation sites with Ga and In. The intermediate indium content values with narrower FWHM are highlighted in red.

concentrations up to x(In) ≤ 0.36 and drops for x(In) = 0.47 and x(In) = 0.59. The line width broadens again for high In concentrations (x(In) > 0.72). The inhomogeneous broadening of radiative recombination in ternary semiconductor materials such as c-$In_xGa_{1-x}N$ is frequently attributed to statistical fluctuations in the composition. The spectral broadening σ_0 is given by $\sigma_0 = (dE_g(x)/dx)\sigma_x$,[55] with x representing the indium content and $E_g(x)$ the composition-dependent band gap. It is known that $\sigma_x^2 = x(1-x)/(cV_{exc})$, where $c = 4a_0^{-3}$ is the cation concentration[56] and $V_{exc} = 10\pi a_{B,x}^2$ is the exciton volume.[55,57,58] Thus, σ_0 then becomes

$$\sigma_0 = \frac{dE_g(x)}{dx}\sqrt{\frac{x(1-x)}{ca_{B,x}}} \quad (4)$$

where $a_{B,x}$ is the Bohr radius within a hydrogen model for recombination, modified by the dielectric constant ε and the effective masses present in the semiconductor.[59] We expect a dependence like the one given by the blue dashed line in Figure 5 if this description holds true for the entire composition range x. While the model describes the observed broadening reasonably well for low and high indium content values, the FWHM values in the intermediate indium content range (0.47 ≤ x(In) ≤ 0.59) are significantly lower than predicted. This composition range (highlighted in red) coincides with the CuPt-type ordering effect that was observed in the HR-HAADF images of the TEM investigation (Figure 3d). Because the ordering effect is on the mesoscopic scale, it has a strong effect on only the emission line width, not on the peak energy. Nevertheless, the results show that the material quality of our c-$In_xGa_{1-x}N$ in the critical composition range of 0.47 ≤ x(In) ≤ 0.59 is sufficient to exhibit radiative recombination.

Preliminary PL experiments also show the emission of our In-rich c-$In_xGa_{1-x}N$ films at room temperature. The intensities of the spectra are about an order of magnitude lower than the ones at 20 K, and the emission maxima shift slightly to lower energies (approximately by 30 meV). Both properties are typical for emissions caused by shallow bound recombination.

Raman spectroscopy monitors the effect In content has on the phonon structure in the films. These dynamic properties of the crystal lattice also reflect the crystal symmetry and, thus, yield additional information about its structural properties, possible phase segregation, or phase transitions. Figure 6

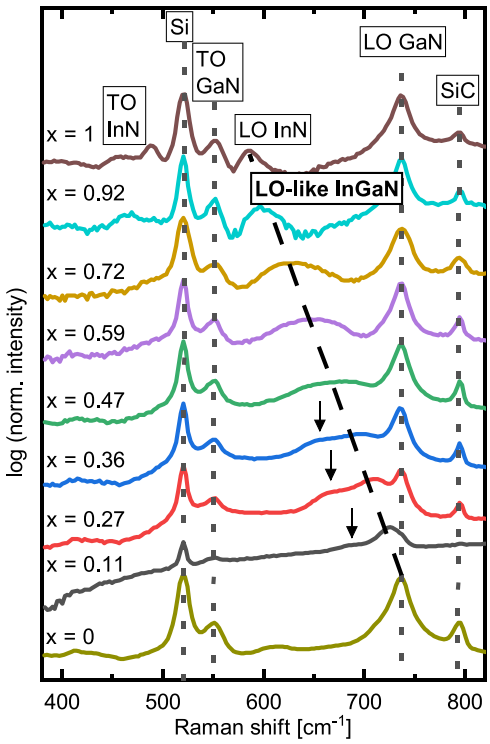

Figure 6. Raman spectra (λ_{exc} = 405 nm) of c-$In_xGa_{1-x}N$ ($0 \le x \le 1$). Substrate peaks are denoted by vertical dotted lines. The c-$In_xGa_{1-x}N$ LO-like mode (black dashed line) shifts with the indium content amount. Black arrows highlight the positions of the secondary peaks that emerge for the low indium content spectra.

depicts the Raman spectra recorded in backscattering geometry from the (001) surfaces of the series of c-$In_xGa_{1-x}N$ layers. The full range of x(In) is covered, and both binary thin films are included as references. However, due to the high penetration depth of the exciting laser light (405 nm), strong buffer and substrate modes are also visible for all x(In) samples, denoted by dashed lines in Figure 6.

The Raman spectra of c-$In_xGa_{1-x}N$ epitaxial layers reveal a Raman signal which shifts linearly with x(In) from c-GaN (737 cm^{-1}[60,61]) to c-InN (586 cm^{-1}[62]). The frequency of this Raman signal is consistent with the longitudinal (LO) phonon frequency in both binary materials. This finding strongly suggests that this semiconductor alloy system exhibits a one-mode behavior that is in accordance with theoretical predictions given by the modified random-element isodisplacement (MREI) model.[63] In addition, a second Raman signal, which also shifts with x(In), is distinguishable in the vicinity of the LO-like signal for In content values in the range of 0.11 ≤ x(In) ≤ 0.36 (indicated by small black arrows in Figure 6). In the In-rich samples (0.47 ≤ x(In) ≤ 0.92), either these two peaks have merged into one broad signal or the LO mode is considerably broadened. In the case of the binary c-InN

https://doi.org/10.1021/acsami.3c06319
ACS Appl. Mater. Interfaces 2023, 15, 39513−39522

epitaxial film, the mode is narrower again. The most commonly given (and often correct) explanation for the broadening of the LO phonon signal is alloy disorder. The origin of additional broad Raman signals, such as the second signal observed here in close vicinity to the LO-like mode of the alloy, is often second-order Raman scattering.[64] However, in our case, it seems unlikely that second-order Raman scattering is the origin of the additional peaks seen here, based on the phonon dispersions calculated for c-GaN and c-InN.[65,66] In our series of samples, preliminary experimental evidence suggests that both effects (i.e., the strong broadening of the LO-like phonon signal at high x(In) and the occurrence of a second signal at lower x(In)) may be related to short-range CuPt-type ordering, which yields alternating In- and Ga-rich lattice planes along the [111] direction. This phenomenon is well-known from $Ga_{1-x}In_xP$ alloys with intermediate x(In).[67,68] The ideal structure that corresponds to the CuPt-type ordering is a rhombohedral crystal structure, where the cubic [111] direction acts as a high symmetry three-fold rotational axis and there is a basis of four atoms (2 N, 1 Ga, 1 In) per unit cell instead of two atoms, as in zincblende crystals. In the idealized structure, the alternating (111) planes of the Ga and In atoms lead to a reduction in the cubic symmetry, accompanied by a doubling of the real space unit cell along the (111) direction. The latter corresponds to a first approximation of a bisection of the zincblende Brillouin zone between the Γ- and L-point. As a result, the zincblende phonon dispersions along this direction are basically folded back to the Γ-point. This means that two LO-like phonons (A_1 symmetry in case of the corresponding rhombohedral structure) become allowed in the presence of CuPt-type ordering. Furthermore, the theoretical work that has been done on phonon dispersions of c-GaN and c-InN[65,66] reports that the LO phonon dispersion of c-InN between Γ and L is flatter than that of c-GaN. This suggests that two LO-like Raman signals are observable at lower In content (as indicated by the arrows in Figure 6) but then merge into one broader feature at higher In content. The frequency difference between the two signals can be estimated from the LO phonon dispersion of the corresponding zincblende material. The frequency difference calculated based on the values for c-GaN is in reasonable agreement with the frequency difference between the two Raman features observed in the spectra.

Although the transverse (TO) modes of zincblende materials are forbidden in the backscattering from (100) surfaces, corresponding modes can be discerned in the spectra of the binary materials at 551 cm^{-1} (c-GaN[60,61,69]) and 458 cm^{-1} (c-InN[62,65,66]). No clear signals can be discerned for the alloy thin films; this is because the anticipated Raman signals are covered by the strong signals of the LO phonon of the Si substrate and the TO mode of the c-GaN buffer layer.

CONCLUSIONS

The present work shows that the miscibility gap of c-GaN and c-InN can be overcome by sophisticated strain management in the MBE growth of cubic c-$In_xGa_{1-x}N$ films on c-GaN/AlN/3C-SiC/Si templates. The substrate temperature governs the indium content, the growth rate, and the morphology of the film. Thorough characterization using HRXRD, Raman spectroscopy, and EDX confirms a singular, partially strained, cubic crystal phase. HR-STEM images reveal a modified CuPt-type ordering in c-$In_xGa_{1-x}N$ when $x \approx 0.5$, which is further supported by the FWHM of the emission line width. Low-temperature photoluminescence demonstrates the tunability of the emission energy from the near-ultraviolet to the near-infrared with a bowing coefficient of 2.4 eV. Our results encourage further efforts toward device fabrication including electrical characterization and thermal stability, as well as the growth of quantum structures for a higher emission yield and spectral optimizations.

ASSOCIATED CONTENT

Supporting Information

The Supporting Information is available free of charge at https://pubs.acs.org/doi/10.1021/acsami.3c06319.

Figure S1: RHEED images of samples grown at high and low growth temperatures. Figure S2: HR-STEM image of a c-$In_xGa_{1-x}N$ layer with x(In) = 0.21 (PDF)

AUTHOR INFORMATION

Corresponding Author

Jörg Schörmann − *Institute of Experimental Physics I and Center for Materials Research, Justus Liebig University Giessen, D-35392 Giessen, Germany;* orcid.org/0000-0001-7244-2201; Email: Joerg.Schoermann@exp1.physik.uni-giessen.de

Authors

Mario Fabian Zscherp − *Institute of Experimental Physics I and Center for Materials Research, Justus Liebig University Giessen, D-35392 Giessen, Germany;* orcid.org/0000-0003-3515-5232

Silas Aurel Jentsch − *Institute of Experimental Physics I and Center for Materials Research, Justus Liebig University Giessen, D-35392 Giessen, Germany*

Marius Johannes Müller − *Institute of Experimental Physics I and Center for Materials Research, Justus Liebig University Giessen, D-35392 Giessen, Germany;* orcid.org/0009-0005-2187-0122

Vitalii Lider − *Materials Science Center and Faculty of Physics, Philipps-University Marburg, D-35032 Marburg, Germany;* orcid.org/0000-0003-4493-9370

Celina Becker − *Materials Science Center and Faculty of Physics, Philipps-University Marburg, D-35032 Marburg, Germany*

Limei Chen − *Institute of Experimental Physics I and Center for Materials Research, Justus Liebig University Giessen, D-35392 Giessen, Germany*

Mario Littmann − *Department of Physics, Paderborn University, D-33098 Paderborn, Germany;* orcid.org/0000-0003-0875-3720

Falco Meier − *Department of Physics, Paderborn University, D-33098 Paderborn, Germany*

Andreas Beyer − *Materials Science Center and Faculty of Physics, Philipps-University Marburg, D-35032 Marburg, Germany;* orcid.org/0000-0001-6533-0631

Detlev Michael Hofmann − *Institute of Experimental Physics I and Center for Materials Research, Justus Liebig University Giessen, D-35392 Giessen, Germany*

Donat Josef As − *Department of Physics, Paderborn University, D-33098 Paderborn, Germany*

Peter Jens Klar − *Institute of Experimental Physics I and Center for Materials Research, Justus Liebig University Giessen, D-35392 Giessen, Germany;* orcid.org/0000-0002-4513-0330

Kerstin Volz − *Materials Science Center and Faculty of Physics, Philipps-University Marburg, D-35032 Marburg, Germany*

Sangam Chatterjee − *Institute of Experimental Physics I and Center for Materials Research, Justus Liebig University Giessen, D-35392 Giessen, Germany;* orcid.org/0000-0002-0237-5880

Complete contact information is available at: https://pubs.acs.org/10.1021/acsami.3c06319

Notes

The authors declare no competing financial interest.

■ ACKNOWLEDGMENTS

Financial support was provided by the German Science Foundation (DFG) through the following schemes: F.M. was supported by DFG Project AS 107/7-1 and M.L. by the transregional collaborative research center TRR 142 project B02, Project 231447078; the authors from Marburg and Giessen acknowledge SFB 1083 (Project 223848855). Additionally, the work was supported through the European Regional Development Fund (ERDF) within the innovation laboratory high-performance materials FPG990 0005/2018.

■ REFERENCES

(1) Binks, D. J.; Dawson, P.; Oliver, R. A.; Wallis, D. J. Cubic GaN and InGaN/GaN Quantum Wells. *Appl. Phys. Rev.* **2022**, *9* (4), 041309.

(2) Feneberg, M.; Röppischer, M.; Cobet, C.; Esser, N.; Schörmann, J.; Schupp, T.; As, D. J.; Hörich, F.; Bläsing, J.; Krost, A.; Goldhahn, R. Optical Properties of Cubic GaN from 1 to 20 eV. *Phys. Rev. B* **2012**, *85* (15), 155207.

(3) Church, S. A.; Hammersley, S.; Mitchell, P. W.; Kappers, M. J.; Sahonta, S. L.; Frentrup, M.; Nilsson, D.; Ward, P. J.; Shaw, L. J.; Wallis, D. J.; Humphreys, C. J.; Oliver, R. A.; Binks, D. J.; Dawson, P. Photoluminescence Studies of Cubic GaN Epilayers. *Phys. Status Solidi Basic Res.* **2017**, *254* (8), 1600733.

(4) Schörmann, J.; As, D. J.; Lischka, K.; Schley, P.; Goldhahn, R.; Li, S. F.; Löffler, W.; Hetterich, M.; Kalt, H. Molecular Beam Epitaxy of Phase Pure Cubic InN. *Appl. Phys. Lett.* **2006**, *89* (26), 261903.

(5) Hsiao, C. L.; Liu, T. W.; Wu, C. T.; Hsu, H. C.; Hsu, G. M.; Chen, L. C.; Shiao, W. Y.; Yang, C. C.; Gällström, A.; Holtz, P. O.; Chen, C. C.; Chen, K. H. High-Phase-Purity Zinc-Blende InN on r-Plane Sapphire Substrate with Controlled Nitridation Pretreatment. *Appl. Phys. Lett.* **2008**, *92* (11), 111914.

(6) Nishida, K.; Kitamura, Y.; Hijikata, Y.; Yaguchi, H.; Yoshida, S. Epitaxial Growth of Hexagonal and Cubic InN Films. *Phys. Status Solidi Basic Res.* **2004**, *241* (12), 2839−2842.

(7) Chichibu, S. F.; Sugiyama, M.; Onuma, T.; Kitamura, T.; Nakanishi, H.; Kuroda, T.; Tackeuchi, A.; Sota, T.; Ishida, Y.; Okumura, H. Localized Exciton Dynamics in Strained Cubic In0.1Ga0.9N/GaN Multiple Quantum Wells. *Appl. Phys. Lett.* **2001**, *79* (26), 4319.

(8) Church, S. A.; Quinn, M.; Cooley-Greene, K.; Ding, B.; Gundimeda, A.; Kappers, M. J.; Frentrup, M.; Wallis, D. J.; Oliver, R. A.; Binks, D. J. Photoluminescence Efficiency of Zincblende InGaN/GaN Quantum Wells. *J. Appl. Phys.* **2021**, *129* (17), 175702 DOI: 10.1063/5.0046649.

(9) Schörmann, J.; Potthast, S.; As, D. J.; Lischka, K. Near Ultraviolet Emission from Nonpolar Cubic AlxGa1-xN/GaN Quantum Wells. *Appl. Phys. Lett.* **2006**, *89* (13), No. 131910.

(10) Li, S.; Schörmann, J.; As, D. J.; Lischka, K. Room Temperature Green Light Emission from Nonpolar Cubic InGaN/GaN Multi-Quantum-Wells. *Appl. Phys. Lett.* **2007**, *90* (7), No. 071903.

(11) Tsai, Y. C.; Leburton, J. P.; Bayram, C. Quenching of the Efficiency Droop in Cubic Phase InGaAlN Light-Emitting Diodes. *IEEE Trans. Electron Devices* **2022**, *69* (6), 3240−3245.

(12) Novikov, S. V.; Zainal, N.; Akimov, A. V.; Staddon, C. R.; Kent, A. J.; Foxon, C. T. Molecular Beam Epitaxy as a Method for the Growth of Freestanding Zinc-Blende (Cubic) GaN Layers and Substrates. *J. Vac. Sci. Technol. B, Nanotechnol. Microelectron. Mater. Process. Meas. Phenom.* **2010**, *28* (3), C3B1−C3B6.

(13) Teles, L. K.; Furthmuller, J.; Scolfaro, L. M. R.; Tabata, A.; Leite, J. R.; Bechstedt, F.; Frey, T.; As, D. J.; Lischka, K. Phase Separation and Gap Bowing in Zinc-Blende InGaN, InAlN, BGaN, and BAlN Alloy Layers. *Phys. E* **2002**, *13*, 1086−1089.

(14) Ferhat, M.; Bechstedt, F. First-Principles Calculations of Gap Bowing in InxGa1-xN and InxAl1-xN Alloys: Relation to Structural and Thermodynamic Properties. *Phys. Rev. B* **2002**, *65* (7), 1−7.

(15) Husberg, O.; Khartchenko, A.; As, D. J.; Vogelsang, H.; Frey, T.; Schikora, D.; Lischka, K.; Noriega, O. C.; Tabata, A.; Leite, J. R. Photoluminescence from Quantum Dots in Cubic GaN/InGaN/GaN Double Heterostructures. *Appl. Phys. Lett.* **2001**, *79* (9), 1243−1245.

(16) Husberg, O.; Khartchenko, A.; As, D. J.; Lischka, K.; Silveira, E.; Noriega, O. C.; Fernandez, J. R. L.; Leite, J. R. Thermal Annealing of Cubic-InGaN/GaN Double Heterostructures. *phys. stat. sol. (c)* **2002**, *0* (1), 293−297.

(17) Silveira, E.; Tabata, A.; Leite, J. R.; Trentin, R.; Lemos, V.; Frey, T.; As, D. J.; Schikora, D.; Lischka, K. Evidence of Phase Separation in Cubic InxGa1-xN Epitaxial Layers by Resonant Raman Scattering. *Appl. Phys. Lett.* **1999**, *75* (23), 3602.

(18) Zscherp, M. F.; Mengel, N.; Hofmann, D. M.; Lider, V.; Ojaghi Dogahe, B.; Becker, C.; Beyer, A.; Volz, K.; Schörmann, J.; Chatterjee, S. AlN Buffer Enhances the Layer Quality of MBE-Grown Cubic GaN on 3C-SiC. *Cryst. Growth Des.* **2022**, *22* (11), 6786−6791.

(19) Schörmann, J.; Potthast, S.; As, D. J.; Lischka, K. In Situ Growth Regime Characterization of Cubic GaN Using Reflection High Energy Electron Diffraction. *Appl. Phys. Lett.* **2007**, *90* (4), No. 041918.

(20) Zscherp, M. F.; Jentsch, S. A.; Müller, M. J.; Littmann, M.; Meier, F.; Hofmann, D. M.; As, D. J.; Chatterjee, S.; Schörmann, J. Growth of Cubic InxGa1-xN over Whole Composition by MBE. *Proc. SPIE 12421, Gall. Nitride Mater. Devices XVIII* **2023**, *12421* (March), 78−83.

(21) Dunstan, D. J. Strain and Strain Relaxation in Semiconductors. *J. Mater. Sci. Mater. Electron.* **1997**, *8*, 337−375.

(22) Frentrup, M.; Lee, L. Y.; Sahonta, S. L.; Kappers, M. J.; Massabuau, F.; Gupta, P.; Oliver, R. A.; Humphreys, C. J.; Wallis, D. J. X-Ray Diffraction Analysis of Cubic Zincblende III-Nitrides. *J. Phys. D. Appl. Phys.* **2017**, *50* (43), 433002.

(23) Wright, A. F. Elastic Properties of Zinc-Blende and Wurtzite AlN, GaN, and InN. *J. Appl. Phys.* **1997**, *82* (6), 2833−2839.

(24) Vurgaftman, I.; Meyer, J. R. Band Parameters for Nitrogen-Containing Semiconductors. *J. Appl. Phys.* **2003**, *94* (6), 3675−3696.

(25) Tabata, A.; Teles, L. K.; Scolfaro, L. M. R.; Leite, J. R.; Kharchenko, A.; Frey, T.; As, D. J.; Schikora, D.; Lischka, K.; Furthmüller, J.; Bechstedt, F. Phase Separation Suppression in InGaN Epitaxial Layers Due to Biaxial Strain. *Appl. Phys. Lett.* **2002**, *80* (5), 769−771.

(26) Kemper, R. M.; Veit, P.; Mietze, C.; Dempewolf, A.; Wecker, T.; Bertram, F.; Christen, J.; Lindner, J. K. N.; As, D. J. STEM-CL Investigations on the Influence of Stacking Faults on the Optical Emission of Cubic GaN Epilayers and Cubic GaN/AlN Multi-Quantum Wells. *Phys. Status Solidi Curr. Top. Solid State Phys.* **2015**, *12* (4−5), 469−472.

(27) Martinez-Guerrero, E.; Bellet-Amalric, E.; Martinet, L.; Feuillet, G.; Daudin, B.; Mariette, H.; Holliger, P.; Dubois, C.; Bru-Chevallier, C.; Nze, P. A.; Chassagne, T.; Ferro, G.; Monteil, Y. Structural Properties of Undoped and Doped Cubic GaN Grown on SiC(001). *J. Appl. Phys.* **2002**, *91* (8), 4983−4987.

(28) Lee, L. Y.; Frentrup, M.; Vacek, P.; Kappers, M. J.; Wallis, D. J.; Oliver, R. A. Investigation of Stacking Faults in MOVPE-Grown

Zincblende GaN by XRD and TEM. *J. Appl. Phys.* **2019**, *125* (10), No. 105303.
(29) Vacek, P.; Frentrup, M.; Lee, L. Y.; Massabuau, F. C. P.; Kappers, M. J.; Wallis, D. J.; Gröger, R.; Oliver, R. A. Defect Structures in (001) Zincblende GaN/3C-SiC Nucleation Layers. *J. Appl. Phys.* **2021**, *129* (15), 155306 DOI: 10.1063/5.0036366.
(30) Johansson, C. H.; Linde, J. O. Gitterstruktur und elektrisches Leitvermögen der Mischkristallreihen Au-Cu, Pd-Cu und Pt-Cu. *Ann. Phys.* **1927**, *387* (4), 449−478.
(31) Walker, C. B. X-Ray Measurement of Order in CuPt. *J. Appl. Phys.* **1952**, *23* (1), 118−123.
(32) Jen, H. R.; Ma, K. Y.; Stringfellow, G. B. Long-Range Order in InAsSb. *Appl. Phys. Lett.* **1989**, *54* (12), 1154−1156.
(33) Srivastava, G. P.; Martins, J. L.; Zunger, A. Atomic Structure and Ordering in Semiconductor Alloys. *Phys. Rev. B* **1985**, *31* (4), 2561−2564.
(34) Bellon, P.; Chevalier, J. P.; Martin, G. P.; Dupont-Nivet, E.; Thiebaut, C.; Andre, J. P. Chemical Ordering in GaxIn1−xP Semiconductor Alloy Grown by Metalorganic Vapor Phase Epitaxy. *Appl. Phys. Lett.* **1988**, *52* (7), 567−569.
(35) Kondow, M.; Kakibayashi, H.; Minagawa, S. ORDERED STRUCTURE IN OMVPE-GROWN Ga0.5In0.5P. *J. Cryst. Growth* **1988**, *88*, 291−296.
(36) Teles, L. K.; Ferreira, L. G.; Leite, J. R.; Scolfaro, L. M. R.; Kharchenko, A.; Husberg, O.; As, D. J.; Schikora, D.; Lischka, K. Strain-Induced Ordering in InxGa1-xN Alloys. *Appl. Phys. Lett.* **2003**, *82* (24), 4274−4276.
(37) Teles, L. K.; Marques, M.; Ferreira, L. G.; Scolfaro, L. M. R.; Leite, J. R. Phase Separation, Effects of Biaxial Strain, and Ordered Phase Formations in Cubic Nitride Alloys. *Microelectronics J.* **2004**, *35*, 53−57.
(38) Islam, M. R.; Kaysir, M. R.; Islam, M. J.; Hashimoto, A.; Yamamoto, A. MOVPE Growth of InxGa1-xN (x ∼ 0.4) and Fabrication of Homo-Junction Solar Cells. *J. Mater. Sci. Technol.* **2013**, *29* (2), 128−136.
(39) Kazazis, S. A.; Papadomanolaki, E.; Androulidaki, M.; Kayambaki, M.; Iliopoulos, E. Optical Properties of InGaN Thin Films in the Entire Composition Range. *J. Appl. Phys.* **2018**, *123* (12), 125101 DOI: 10.1063/1.5020988.
(40) Moret, M.; Gil, B.; Ruffenach, S.; Briot, O.; Giesen, C.; Heuken, M.; Rushworth, S.; Leese, T.; Succi, M. Optical, Structural Investigations and Band-Gap Bowing Parameter of GaInN Alloys. *J. Cryst. Growth* **2009**, *311* (10), 2795−2797.
(41) Compeán García, V. D.; Orozco Hinostroza, I. E.; Escobosa Echavarría, A.; López Luna, E.; Rodríguez, A. G.; Vidal, M. A. Bulk Lattice Parameter and Band Gap of Cubic InxGa1-xN (001) Alloys on MgO (100) Substrates. *J. Cryst. Growth* **2015**, *418*, 120−125.
(42) Brandt, O.; Müllhaüser, J. R.; Trampert, A.; Ploog, K. H. Properties of Cubic (In,Ga)N Grown by Molecular Beam Epitaxy. *Mater. Sci. Eng., B* **1999**, *59* (1−3), 73−79.
(43) Lemos, V.; Silveira, E.; Leite, J. R.; Tabata, A.; Trentin, R.; Scolfaro, L. M. R.; Frey, T.; As, D. J.; Schikora, D.; Lischka, K. Evidence for Phase-Separated Quantum Dots in Cubic InGaN Layers from Resonant Raman Scattering. *Phys. Rev. Lett.* **2000**, *84* (16), 3666−3669.
(44) Chichibu, S. F.; Sugiyama, M.; Kuroda, T.; Tackeuchi, A.; Kitamura, T.; Nakanishi, H.; Sota, T.; DenBaars, S. P.; Nakamura, S.; Ishida, Y.; Okumura, H. Band Gap Bowing and Exciton Localization in Strained Cubic InxGa1-xN Films Grown on 3C-SiC (001) by Rf Molecular-Beam Epitaxy. *Appl. Phys. Lett.* **2001**, *79* (22), 3600−3602.
(45) Goldhahn, R.; Scheiner, J.; Shokhovets, S.; Frey, T.; Köhler, U.; As, D. J.; Lischka, K. Refractive Index and Gap Energy of Cubic InxGa1-xN. *Appl. Phys. Lett.* **2000**, *76* (3), 291−293.
(46) Kitamura, T.; Cho, S. H.; Ishida, Y.; Ide, T.; Shen, X. Q.; Nakanishi, H.; Chichibu, S.; Okumura, H. Growth and Characterization of Cubic InGaN Epilayers on 3C-SiC by RF MBE. *J. Cryst. Growth* **2001**, *227*−*228*, 471−475.
(47) Müllhäuser, J. R.; Jenichen, B.; Wassermeier, M.; Brandt, O.; Ploog, K. H. Characterization of Zinc Blende InxGa1-xN Grown by Radio Frequency Plasma Assisted Molecular Beam Epitaxy on GaAs (001). *Appl. Phys. Lett.* **1997**, *71* (7), 909−911.
(48) Sun, X. L.; Wang, Y. T.; Yang, H.; Zheng, L. X.; Xu, D. P.; Li, J. B.; Wang, Z. G. Strain and Photoluminescence Characterization of Cubic (In,Ga) N Films Grown on GaAs(001) Substrates. *J. Appl. Phys.* **2000**, *87* (8), 3711−3714.
(49) Holst, J.; Hoffmann, A.; Rudloff, D.; Bertram, F.; Riemann, T.; Christen, J.; Frey, T.; As, D. J.; Schikora, D.; Lischka, K. The Origin of Optical Gain in Cubic InGaN Grown by Molecular Beam Epitaxy. *Appl. Phys. Lett.* **2000**, *76* (20), 2832−2834.
(50) Pacheco-Salazar, D. G.; Leite, J. R.; Cerdeira, F.; Meneses, E. A.; Li, S. F.; As, D. J.; Lischka, K. Photoluminescence Measurements on Cubic InGaN Layers Deposited on a SiC Substrate. *Semicond. Sci. Technol.* **2006**, *21* (7), 846−851.
(51) Orozco Hinostroza, I. E.; Avalos-Borja, M.; Compeán García, V. D.; Zamora, C. C.; Rodríguez, A. G.; López Luna, E.; Vidal, M. A. Tuning Emission in Violet, Blue, Green and Red in Cubic GaN/InGaN/GaN Quantum Wells. *J. Cryst. Growth* **2016**, *435*, 110−113.
(52) Chichibu, S. F.; Setoguchi, A.; Azuhata, T.; Müllhäuser, J.; Sugiyama, M.; Mizutani, T.; Deguchi, T.; Nakanishi, H.; Sota, T.; Brandt, O.; Ploog, K. H.; Mukai, T.; Nakamura, S. Effective Localization of Quantum Well Excitons in InGaN Quantum Well Structures with High InN Mole Fraction. *phys. stat. sol. (a)* **2000**, *180*, 321−325.
(53) Compean-Garcia, V.D.; Hernandez-Vazquez, O.; Garcia-Hernandez, S.A.; Luna, E.L.; Vidal, M.A. Critical Thickness as a Function of the Indium Molar Fraction in Cubic InxGa1-xN and the Influence in the Growth of Nanostructures. *Mater. Sci. Semicond. Process.* **2020**, *115*, 105101.
(54) Vilchis, H.; Compeán-García, V. D.; Orozco-Hinostroza, I. E.; López-Luna, E.; Vidal, M. A.; Rodríguez, A. G. Complex Refractive Index of InxGa1-xN Thin Films Grown on Cubic (100) GaN/MgO. *Thin Solid Films* **2017**, *626*, 55−59.
(55) Grundmann, M.; Dietrich, C. P. Lineshape Theory of Photoluminescence from Semiconductor Alloys. *J. Appl. Phys.* **2009**, *106* (12), No. 123521.
(56) Schubert, E. F.; Göbel, E. O.; Horikoshi, Y.; Ploog, K.; Queisser, H. J. Alloy Broadening in Photoluminescence Spectra of AlxGa1-xAs. *Phys. Rev. B* **1984**, *30* (2), 813−820.
(57) Goede, O.; John, L.; Hennig, D. Compositional Disorder-Induced Broadening for Free Excitons in II-VI Semiconducting Mixed Crystals. *Phys. stat. sol. b* **1978**, *89*, K183.
(58) Zimmermann, R. Theory of Exciton Linewidth in II-VI Semiconductor Mixed Crystals. *J. Cryst. Growth* **1990**, *101* (1−4), 346−349.
(59) Fritsch, D.; Schmidt, H.; Grundmann, M. Band-Structure Pseudopotential Calculation of Zinc-Blende and Wurtzite AlN, GaN, and InN. *Phys. Rev. B - Condens. Matter Mater. Phys.* **2003**, *67* (23), 1−13.
(60) Yaguchi, H.; Wu, J.; Zhang, B.; Segawa, Y.; Nagasawa, H.; Onabe, K.; Shiraki, Y. Micro Raman and Micro Photoluminescence Study of Cubic GaN Grown on 3C-SiC(0 0 1) Substrates by Metalorganic Vapor Phase Epitaxy. *J. Cryst. Growth* **1998**, *195* (1−4), 323−327.
(61) Giehler, M.; Ramsteiner, M.; Brandt, O.; Yang, H.; Ploog, K. H. Optical Phonons of Hexagonal and Cubic GaN Studied by Infrared Transmission and Raman Spectroscopy. *Appl. Phys. Lett.* **1995**, *67* (6), 733−735.
(62) Tabata, A.; Lima, A. P.; Teles, L. K.; Scolfaro, L. M. R.; Leite, J. R.; Lemos, V.; Schöttker, B.; Frey, T.; Schikora, D.; Lischka, K. Structural Properties and Raman Modes of Zinc Blende InN Epitaxial Layers. *Appl. Phys. Lett.* **1999**, *74* (3), 362−364.
(63) Grille, H.; Schnittler, C.; Bechstedt, F. Phonons in Ternary Group-III Nitride Alloys. *Phys. Rev. B - Condens. Matter Mater. Phys.* **2000**, *61* (9), 6091−6105.
(64) Haboeck, U.; Siegle, H.; Hoffmann, A.; Thomsen, C. Lattice Dynamics in GaN and AlN Probed with First- and Second-Order Raman Spectroscopy. *Phys. Status Solidi C* **2003**, *0* (6), 1710−1731.

(65) Xia, H.; Feng, Y.; Patterson, R.; Jia, X.; Shrestha, S.; Conibeer, G. Theoretical Calculation of the Vibrational and Thermal Properties of Wurtzite InN-GaN Multiple Quantum Well Superlattice. *J. Appl. Phys.* **2013**, *113* (16), 164304.
(66) Bağci, S.; Duman, S.; Tütüncü, H. M.; Srivastava, G. P. Ab Initio Calculations of Phonon Dispersion Relations for Bulk and (1 1 0) Surface of Cubic InN. *J. Phys. Chem. Solids* **2009**, *70* (2), 444−450.
(67) Gant, T. A.; Dutta, M.; El-Masry, N. A.; Bedair, S. M.; Stroscio, M. A. Raman Study of Ordering in Ga1-xInxP. *Phys. Rev. B* **1992**, *46* (7), 3834−3838.
(68) Mintairov, A. M.; Merz, J. L.; Vlasov, A. S.; Vinokurov, D. V. Observation of a Martensitic Transition in the Raman Spectra of Spontaneously Ordered GaInP Alloys. *Semicond. Sci. Technol.* **1998**, *13* (10), 1140−1147.
(69) Baron, E.; Feneberg, M.; Goldhahn, R.; Deppe, M.; Tacken, F.; As, D. J. Optical Evidence of Many-Body Effects in the Zincblende AlxGa1-xN Alloy System. *J. Phys. D. Appl. Phys.* **2021**, *54* (2), 025101.

https://doi.org/10.1021/acsami.3c06319
ACS Appl. Mater. Interfaces 2023, 15, 39513−39522